

Comparison of Velocity Estimates From Advanced Very High Resolution Radiometer in the Coastal Transition Zone

KATHRYN A. KELLY

Woods Hole Oceanographic Institution, Woods Hole, Massachusetts

P. TED STRUB

College of Oceanography, Oregon State University, Corvallis

Two methods of estimating surface velocity vectors from advanced very high resolution radiometer (AVHRR) data were applied to the same set of images and the results were compared with in situ and altimeter measurements. The first method used an automated feature-tracking algorithm and the second method used an inversion of the heat equation. The 11 images were from 3 days in July 1988 during the Coastal Transition Zone field program and the in situ data included acoustic Doppler current profiler (ADCP) vectors and velocities from near-surface drifters. The two methods were comparable in their degree of agreement with the in situ data, yielding velocity magnitudes that were 30–50% less than drifter and ADCP velocities measured at 15–20 m depth, with rms directional differences of about 60°. These differences compared favorably with a baseline difference estimate between ADCP vectors interpolated to drifter locations within a well-sampled region. High correlations between the AVHRR estimates and the coincident Geosat geostrophic velocity profiles suggested that the AVHRR methods adequately resolved the important flow features. The flow field was determined to consist primarily of a meandering southward flowing current, interacting with several eddies, including a strong anticyclonic eddy to the north of the jet. Incorporation of sparse altimeter data into the AVHRR estimates gave a modest improvement in comparisons with in situ data.

1. INTRODUCTION

The prospect of obtaining time series of velocity maps of the ocean without having to make extensive field measurements has prompted numerous attempts to infer the surface velocity field from satellite image data. These fields represent nearly instantaneous estimates of the currents over a large area, avoiding the temporal aliasing inherent in ship surveys. Methods to infer the velocity field from images of sea surface temperature (SST) fall into two categories: those which follow features in the field without regard to the actual temperatures [e.g., *Vastano and Borders*, 1984; *Emery et al.*, 1986; *Tokmakian et al.*, 1990] and those which use the heat equation and the measured SST [e.g., *Kelly*, 1983, 1989; *Wald*, 1983]. The advantage of the first type is that it does not require precise temperatures and therefore the results are less sensitive to errors in the data. Inversion of the data using the heat equation requires a correction for water vapor or viewing geometry. As a by-product, the analysis using the heat equation produces an estimate of the SST changes due to horizontal advection of heat in the upper ocean.

To evaluate and compare these two methods we have used them independently and in combination on a series of advanced very high resolution radiometer (AVHRR) images from the Coastal Transition Zone (CTZ) experiment [*Brink and Cowles*, 1991]. The images were from an unusually cloud-free period, spanning about 3 days in July 1988, and thus represent the best possible data conditions.

There were also numerous field measurements with which to compare the estimates, primarily from the acoustic Doppler current profiler (ADCP) and surface drifters (drogued to 15 m) [*Huyer et al.*, 1991; *Brink et al.*, 1991]. In addition, the Geosat altimeter provided estimates of the anomalous geostrophic velocity, relative to the 2.5-year mean velocity. Although the altimeter gives only one component of the velocity, it has the advantage of sampling the field systematically along the tracks, unlike the drifters, which tend to be drawn into and oversample the most energetic jets. Although the primary focus of this analysis is the comparison of the two methods of using AVHRR sequences, we also looked at combining the two methods with each other and with other satellite or in situ data.

The two methods for estimating the velocities are the maximum cross correlation (MCC) method of *Emery et al.* [1986] and a modified version of the *Kelly* [1989] inversion. The data used in the comparison are described in section 2, followed by a brief description of the methods in section 3, with emphasis on the modifications to the original methods. In section 4 we evaluate the velocity estimates by comparison with other data. Also in section 4 we describe the combination of AVHRR and other velocities using both objective analysis and the inversion of the heat equation. Section 5 contains a discussion of the interpretation of the velocity estimates and their usefulness. The last section contains the summary and conclusions. The viewing angle correction for SST for the heat equation inversion is discussed in Appendix A and further details of the methods are presented in Appendices B and C.

Copyright 1992 by the American Geophysical Union.

2. DATA PROCESSING

The AVHRR images covered the region from 34.5°N to 39.5°N and from 122.3°W to 129.0°W during the period

from July 16 through July 18 (year days 198–200 in 1988). Figure 1 shows one image from July 17 with velocities from surface drifters superimposed. The drifters and field surveys from this period showed a strong jet that flowed toward the southwest, from the northeast corner of the survey region (39.0°N, 124.3°W, 50 km from the coast) to approximately 36.5°N, 127.5°W (an offshore extent of approximately 300 km), where it turned cyclonically and flowed back onshore and to the south, forming a large meander [Huyer *et al.*, 1991; Brink *et al.*, 1991; Strub *et al.*, 1991]. A closed cyclonic eddy (diameter less than 100 km) was found inshore of the cyclonic meander at 37°N and 126.5°W, and a larger (150-km diameter) anticyclonic eddy was traced by a surface drifter at approximately 35.5°N, 124°W [Strub *et al.*, 1991]. ADCP velocity transects across the jet near 125°W revealed velocities as large as 0.8 m s^{-1} in the 20 to 40-km-wide core of the jet [Dewey *et al.*, 1991]. Surface drifters were apparently drawn by converging flow into an even narrower and more energetic core, where velocities as large as 1.2 m s^{-1} were encountered [Swenson *et al.*, 1992]. The coldest water was often found in a narrow filament just inshore of the maximum velocities in the jet's core [Huyer *et al.*, 1991; Chavez *et al.*, 1991; Strub *et al.*, 1991].

Images from the polar-orbiting NOAA 9 and NOAA 10 satellites were converted to brightness temperatures using only the channel 4 (10.3–11.3 μm) radiances. A total of 11 images from July 1988 were processed; the times of the images (year day and hour in UT) are given in Table 1. Images were registered to a common equirectangular projection, using the coordinates of known coastal features to correct the navigation to within approximately one pixel (1.08 km square). Although clouds in the data are a problem for either method of estimating the velocity, these images were relatively cloud free and no explicit cloud flagging was

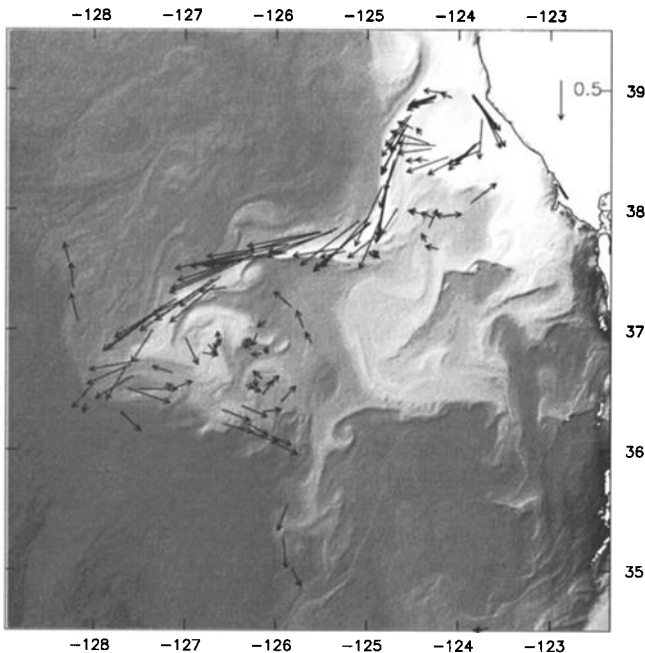


Fig. 1. SST from the AVHRR image on July 17, 1707 UT (image F, Table 1), overlaid with drifter velocities from three of the five 12-hour periods used for comparison with the AVHRR-derived velocities. The scale arrow shows the length of a vector representing 0.5 m s^{-1} . Lighter gray shades correspond to cooler temperatures.

TABLE 1. AVHRR Images Used in the Velocity Estimates

	Year Day:Hour 1988, UT
A	198:12
B	198:15
C	198:23
D	199:03
E	199:12
F	199:17
G	199:23
H	200:02
I	200:11
J	200:16
K	200:23

done. However, some cloud contamination was present, and simple screening methods were used to discount the velocity estimates in these regions. The heat equation requires relatively accurate SST gradients. Following Kelly and Davis [1986], a simple viewing angle correction for water vapor was applied to the channel 4 data (see Appendix A). This correction removed trends in the mean and the variance of SST in the series of images (see Table A1); however considerable scatter remained in the SST variance for the series of images after the correction was applied.

Only two profiles (Figure 2) from the Geosat altimeter Exact Repeat Mission (ERM) were used for comparison with the velocity estimates, because the sampling interval (17 days) of the altimeter was so much larger than the interval over which velocity estimates were computed (2.5 days) and because only the ascending subtracks of the altimeter

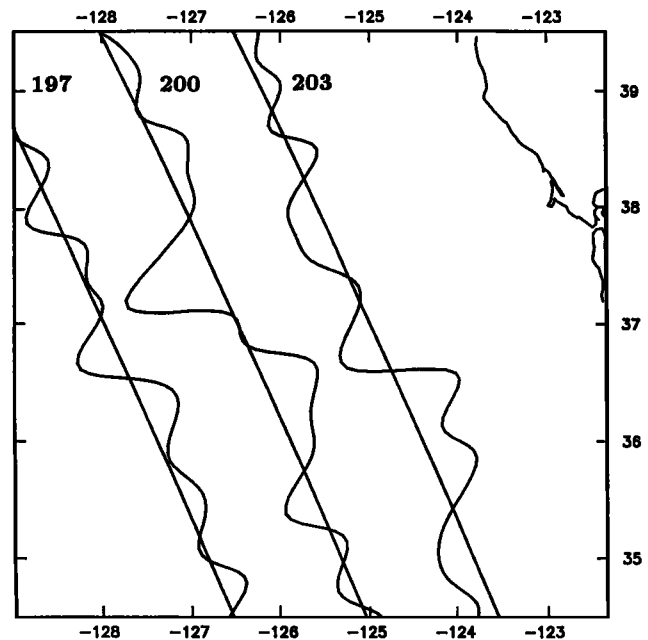


Fig. 2. Ascending subtracks of the Geosat altimeter. The cross-track component of geostrophic velocity, derived from the residual sea surface height profiles, is plotted with positive (onshore) velocity toward the right. Only the three profiles from days 197, 200 and 203 were used in the comparisons with the velocity solutions. Maximum speed is about 0.67 m s^{-1} .

contained usable data. These profiles were separated by approximately 100 km in space and 3 days in time; the dates for the profiles were days 200 and 203. Profiles for days 197 and 206 were available, but the low correlations between the velocity estimates and these profiles suggested that the temporal separation was too large for them to be useful.

Collinear height profiles for the 2.5-year ERM were processed using programs described by *Caruso et al.* [1990] to obtain a series of anomalous sea surface heights. Raw altimeter heights were adjusted for tides, water vapor, tropospheric and ionospheric delays, and surface pressure using correction factors provided on the National Oceanographic Data Center (NODC) distribution tapes [*Cheney et al.*, 1987]. For each subtrack all of the profiles were interpolated to a common latitude-longitude grid with points separated by 0.98 s (approximately 7 km) alongtrack. Orbit errors over approximately 30° arcs were removed using a least squares fit to a sine function, with period equal to the orbital period of the satellite. The mean of all the height profiles for each subtrack was removed, and the anomalous sea surface height was low-pass filtered using a filter with a half-power point of 55 km to reduce instrument noise. Filtered anomalous sea surface height h was converted to anomalous cross-track velocity u , assuming the geostrophic relationship

$$u = \frac{-g}{f} \frac{\partial h}{\partial y} \quad (1)$$

where y is the alongtrack coordinate, g is gravity, and f is the Coriolis parameter. The anomalous geostrophic velocity profiles are shown in Figure 2, with positive (onshore) cross-track velocities to the right. The maximum offshore jet velocity calculated in this manner was 0.67 m s^{-1} ; this maximum is relatively low, probably because the half-power point for the spatial filter is larger than the jet width of 20–40 km.

The CTZ field program used Tristar Mark II drifters [*Niiler et al.*, 1987] with 6-m radar reflector-shaped drogues at a central depth of 15 m. Positions of the drifters were determined eight times each day using the Argos satellite system, with an accuracy of approximately 300 m for each position. The drifters are thought to follow horizontal currents with root-mean-square (rms) errors of only 0.01 m s^{-1} under normal conditions. The drifter positions over intervals of 4 days were fit to cubic splines to remove inertial and tidal signals. This procedure is equivalent to temporal smoothing with a half-power point of 0.45 cpd [*Brink et al.*, 1991]. The final data set consisted of positions separated by 12 hours. Velocity vectors were calculated from pairs of these positions with nominal times at the midpoint of the time interval and locations at the midpoint of the two positions. The drifter velocities for the first three 12-hour periods used in the comparisons are shown in Figure 1.

ADCP data were collected by two ships using hull-mounted transducers: a 300-kHz transducer on the R/V *Wecoma* and a 150-kHz transducer on the R/V *Point Sur*. Navigation data from LORAN-C receivers were used on each ship to convert the relative velocity from the ADCP to absolute current and ship velocities [*Kosro et al.*, 1991]. The currents were filtered to remove signals with periods less than 30 minutes and averaged horizontally over 20-km bins. The top two bins used here were centered at 15.1 m and 19.1 m depth for the *Wecoma* and 16.7 m and 20.7 m for

the *Point Sur*. The ADCP data collected over the 2.5-day period at the nominal 20-m depth are shown in Figure 3. A comparison of the altimeter, drifter and ADCP velocities shows the more uniform spatial sampling of the altimeter and ADCP data, the relatively small region covered by the ADCP data, and the oversampling of the narrow jet by the drifters.

3. ANALYSIS METHODS

To compare the velocity estimates from the two different methods with each other and with the data, we defined five non-overlapping time intervals, each 12 hours long, beginning at noon UT on day 198. A best possible velocity estimate for each time interval was computed using each method; these estimates included multiple image pairs for each interval. Because the two methods have slightly different criteria for selecting the best pairs of images, the same pairs of images were not necessarily used for both the MCC and inverse solutions. Most of the estimates used three pairs of images. The two methods are described briefly below with additional details included in the appendices.

MCC Method

The MCC method [*Emery et al.*, 1986] is an automated procedure for estimating the displacements of small regions of SST patterns between sequential AVHRR images. In this procedure a subregion of an initial image is cross correlated with the same size subregion in a subsequent image, searching for the location in the second image which gives the maximum cross-correlation coefficient. The displacement of the water parcel corresponding to the first subregion is assumed to be the distance between its initial location and

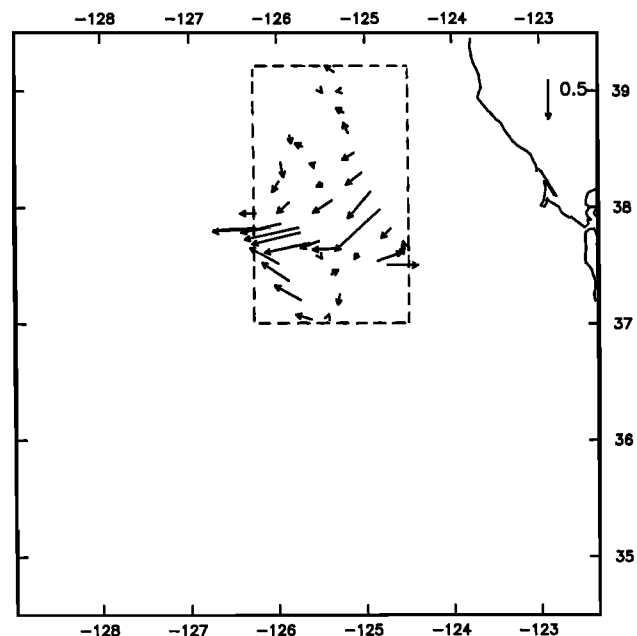


Fig. 3. The ADCP velocity vectors used in the comparison with the velocity solutions from AVHRR. All the individual vectors at a nominal depth of 20 m from the 2.5-day period are shown in the figure. Only those vectors within a 36-hour interval centered on the nominal solution time were used for the comparisons with each velocity solution in Table 2. The ADCP vectors were interpolated to the locations of the drifter vectors which were within the box (dashed line) to obtain baseline error statistics.

the center of the subregion in the second image with the maximum cross correlation. The size of the region searched in the second image (the search window) depends on the maximum displacement that could be caused by reasonable velocities at the ocean surface. The subregion used in the cross-correlation calculation (the correlation tile) should be large enough to contain a number of independent features in the SST field; the number of such features is related to the number of degrees of freedom in the cross-correlation calculation. High-pass filtering the SST field, retaining features smaller than 25 km, increased the number of degrees of freedom by eliminating larger-scale features. Appendix B describes the details of the MCC calculation. Additional

details are given by *Emery et al.* [1986, 1992] and *Garcia and Robinson* [1989]. The correlation tile used here was 25 pixels square and the search window was large enough to accommodate velocities of 1.0 m s^{-1} in any direction (± 10 -30 pixel displacements, depending on the time separations between images). Correlations were empirically determined to be significant with 90% confidence if values of the maximum cross-correlation coefficient r were greater than 0.4 for the 10-pixel search window or 0.6 for the 30-pixel search window.

Once a field of vectors had been produced by the MCC method (Figure 4a), a number of subsequent steps were performed to eliminate obviously erroneous vectors. Vectors as-

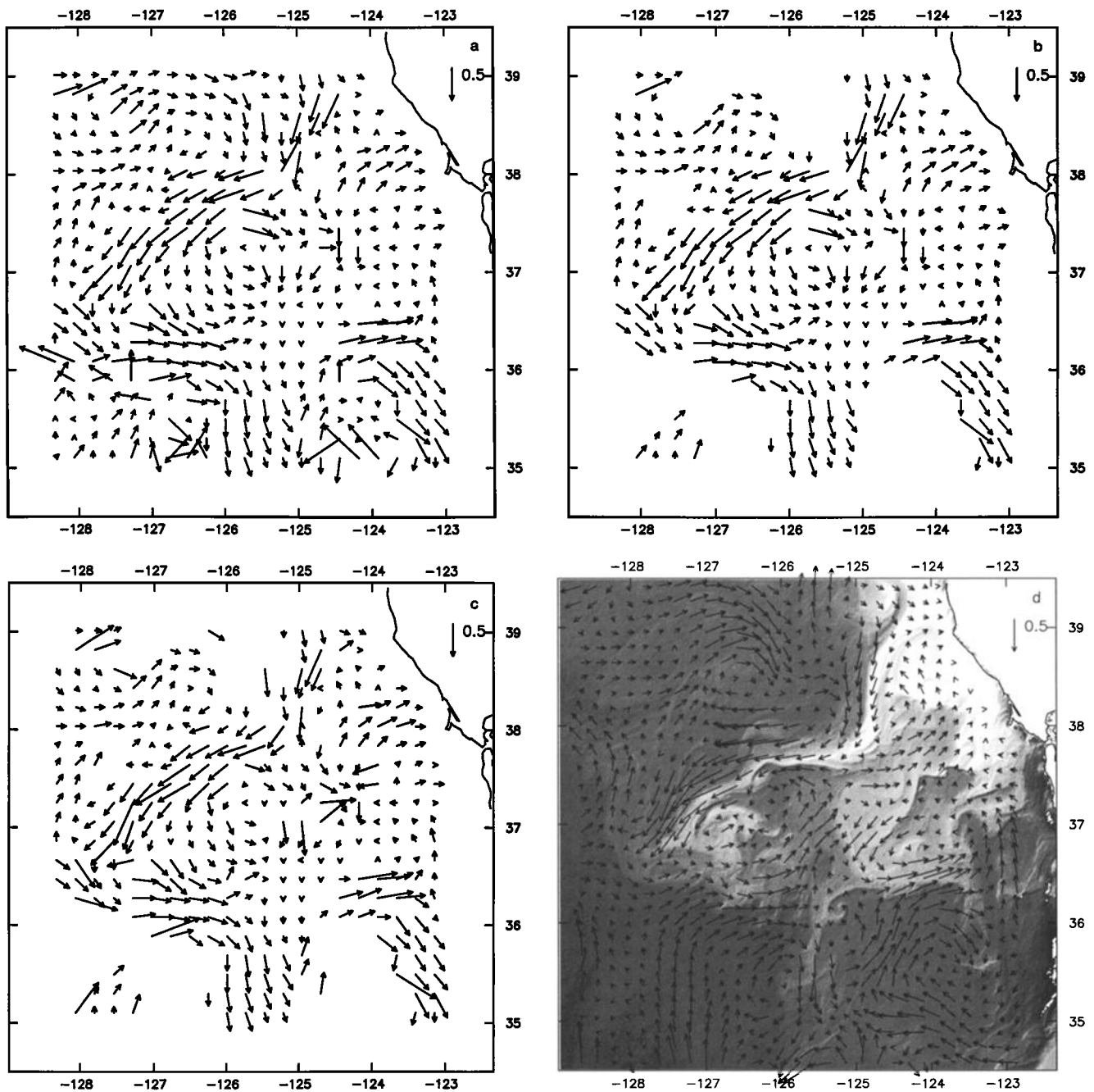


Fig. 4. (a) The full MCC field from the pair of images F and G (Table 1). The vector in the top right shows 0.5 m s^{-1} . (b) The same field as in Figure 4a, after eliminating vectors with cross-correlation coefficient r less than 0.4. (c) As in Figure 4b, after applying a nearest neighbor filter. (d) The weighted average of the fields from the three pairs of images for the third time interval (day 199.75), overlaid on the same AVHRR image as in Figure 1. Each velocity is weighted by r after eliminating individual velocities with r less than 0.4.

sociated with maximum cross correlations less than 0.4 were eliminated, since these values were no greater than random correlations (Figure 4b). A nearest neighbor filter, using a 3×3 subgrid, was used to replace vectors which differed from the subgrid mean by more than 3 standard deviations. The new vector was calculated by searching a 20×20 pixel region around the mean displacement (Figure 4c). After this was done for each pair of images, a weighted average of two or three vector fields was performed, using r for the weighting factor, and excluding vectors with r below the cutoff. For the first three 12-hour periods, three fields were averaged using a cutoff of 0.4, in an attempt to eliminate clouds. Figure 4d shows an average vector field for day 199.75. For the last two 12-hour periods, only two fields were used in the average with the cutoff reduced to 0.1 to keep as many vectors as possible, since there were no apparent clouds.

Inversion of SST Using the Heat Equation

The inversion of the heat equation for the surface velocity field was similar in concept, but differed in detail, from the method described by Kelly [1989]. The heat equation used here is given by

$$T_t + uT_x + vT_y = S(x, y) + m(x, y) \quad (2)$$

where u, v are the horizontal velocity components; T_x, T_y are the horizontal gradients of SST; and T_t is the temporal derivative of SST. The right-hand side of (2) represents SST fluctuations which are due to residual measurement errors, surface heat fluxes, mixing, and vertical advection. We explicitly removed the large spatial scale residual S , which is presumably not due to advection; the smaller-scale residual m is an error term which was minimized in the inversion. Removing the large-scale term in the heat equation is analogous to high-pass filtering the images in the MCC method. Horizontal gradients of SST were computed for 16×16 pixel subsets (16 pixels is approximately 18 km) of the images. The temporal derivatives were computed by finite differences between images, using the average SST for each subset. There is an optimal temporal lag δt between images for the inversion: if δt is too large, the velocity field will change too much from one image to the next or a water parcel will move a distance larger than the subset over which the SST gradient is computed. If, on the other hand, δt is too small, measurement errors will dominate the temporal derivative of SST. The acceptable range of temporal lags was determined by examining the misfit of the best velocity solution to the heat equation; only pairs of images separated by at least 6 hours and by no more than 18 hours were used in the inversions. The preferred value of δt for the inversion is approximately 12 hours, compared with preferred values of 4–6 hours for the MCC method.

The null space of the heat equation (2) contains velocity vectors which are parallel to isotherms as well as any velocity in a region of negligible SST gradients, because these velocity fields do not cause temporal changes in the SST. Kelly [1989] showed that in the absence of any constraint on the solutions, the inversion produced the cross-isotherm velocity component, smoothed by using a limited number of basis functions, but that the addition of a constraint on the solution, such as the minimization of horizontal divergence,

$$\alpha(u_x + v_y = 0) \quad (3)$$

gave plausible total velocity fields. The parameter α is a

weighting factor which determines the importance of this constraint relative to the fit of the velocity solutions to the heat equation (2), which has weight 1.

Several specific changes from Kelly [1989] were made in the inversion method used here and they are discussed in more detail in Appendix C. Two-dimensional biharmonic splines (see, for example, Sandwell, [1987]) were used as basis functions instead of the two-dimensional Fourier series. These splines have an adjustable knot density, so that the solutions behave better in regions of sparse data than functions with a fixed spatial grid. Another change that was made was in the computation of the large-scale temperature change term, which we have called S . To allow more than one pair of images to be used in each inversion, we first removed the S term from each pair of images as a separate calculation, so that the actual form of (2) solved to obtain the velocity field was

$$uT_x + vT_y = -T'_t + m(x, y) \quad (4)$$

where $T'_t = T_t - S(x, y)$ is the residual temperature change after the large-scale contribution S is removed. This change was not incorporated into the inversions by Taggart [1991] on some of the same images because he used only one pair of images in each inversion. A comparison of his results with those obtained here suggested that the use of multiple images qualitatively improved the solutions, particularly in regions of small SST gradients or known cloud contamination.

By varying the weighting parameter α on the divergence, the inversion of the heat equation produces a whole family of solutions. Approximately seven solutions were computed for each time interval with α ranging from 0.005 to 0.32, resulting in solutions with rms speeds of about 0.15–0.60 m s^{-1} and divergences of $1\text{--}15 \times 10^{-6} \text{ s}^{-1}$. The misfit of a solution is defined to be the ratio of the variance of $m(x, y)$ in (4) to the variance of the net temperature change, T'_t , and values for all the computed solutions ranged from 30% to 85%. A consistent set of best solutions was chosen by requiring the solutions for each of the five time intervals to have similar rms speeds and divergence values; the optimal speed and divergence values were determined subjectively to give large jet speeds without large divergences or large vectors near the edges. Figure 5a shows the selected solution for day 199.75 with $\alpha = 0.04$. The solutions which were selected had rms speeds of about 0.23–0.31 m s^{-1} and divergences of $2.7\text{--}5.1 \times 10^{-6} \text{ s}^{-1}$. Although these speeds were somewhat low, as is discussed below, solutions with larger rms speeds did not have a better fit to the comparison data. The misfit to the heat equation varied considerably from one time interval to the next: the misfits of the selected solutions for the five time intervals were 77%, 35%, 34%, 54%, and 76%, respectively.

4. RESULTS

To assess the utility of the AVHRR velocity estimates, we compared them with measured velocities and with each other. All the vectors were measured or estimated at different locations; therefore one set of vectors had to be interpolated in each comparison to the grid of the other set of vectors. For the inverse solution, the spline coefficients define a continuous velocity field, so that the inverse solutions were always interpolated to the location of the data vectors. The MCC vectors, on the other hand, were computed independently at each grid point and thus they had to be

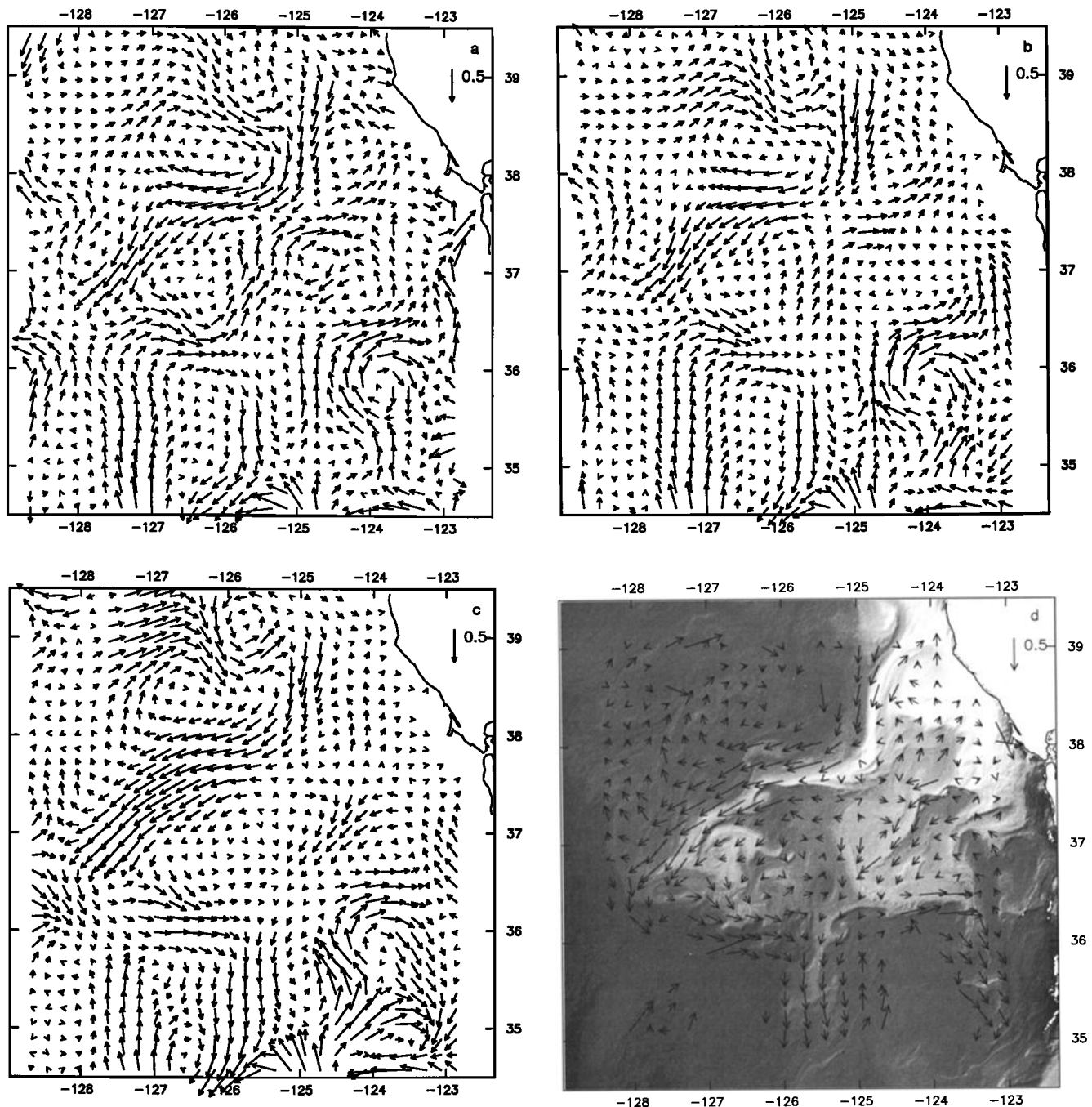


Fig. 5. The selected inverse solution for the third 12-hour period (day 199.75). (a) Full spatial resolution with $\alpha = 0.04$. (b) Reduced spatial resolution with a weight of $\alpha = 0.02$. (c) As in Figure 5b, except including the assimilation of the MCC field from day 199.75 with a weight of $\beta = 0.2$. (d) As in Figure 5b, except including assimilation of the Geosat data along subtracks on days 200 and 203 with weight $\gamma = 0.2$, and overlaid on the same AVHRR image as in Figure 1.

interpolated to the location of the data vectors. All interpolation was done using overdetermined biharmonic splines with $nd = 2$ (see Appendix C); that is, the vectors were smoothed slightly in the interpolation.

For the vector comparisons we chose a measure of misfit which could distinguish between differences in magnitude and differences in direction: the rms ratio of the magnitude of the estimate relative to the data and the rms difference between the directions. To prevent a disproportionately large contribution to the directional difference from very small

vectors, only those vectors with magnitudes larger than 0.05 m s^{-1} were used in the computation. As a baseline estimate for the effect of the interpolation, we interpolated an MCC estimate to its original grid, that is, we simply smoothed it: the ratio of the smoothed magnitudes to the original magnitudes was 0.90 and the rms angular difference was 41° . These values can be used to evaluate the results below: a ratio near 0.90 and an angular difference near 40° are to be expected simply because of the necessary interpolation of vectors to make the comparison.

Comparisons of the AVHRR Velocity Estimates With Data

While none of the more direct velocity measures can be considered the "true" velocity, because each of the measurements has its own sources of error, discrepancies between the AVHRR estimates and a variety of other measurements are suggestive of the nature and magnitude of the errors in the AVHRR estimates. ADCP, drifter, and Geosat data were compared with the velocity estimates for each 12-hour interval. Because there were relatively few ADCP vectors, the vectors from two or three consecutive 12-hour intervals were combined in the comparisons.

To evaluate the differences between the AVHRR velocity estimates and the more direct velocity measurements, we computed a baseline comparison between the ADCP and drifter vectors for the same region. Because the direct measurements were sparse spatially and temporally compared with the AVHRR estimates, we combined direct measurements from the entire period (2.5 days) for the comparison. The ADCP measured in a more regular grid than the drifters; therefore we interpolated the ADCP vectors to the drifter locations which were within the region which was sampled well by the ADCP, as shown in Figure 3. Comparing the interpolated ADCP with the original drifter vectors gave a magnitude ratio (ADCP/drifter) of 0.58 and an rms directional difference of 59°. The small magnitude ratio, relative to the approximately 0.90 ratio expected from interpolation alone, demonstrates that the drifter speeds are systematically larger than those from the ADCP. There are a variety of reasons why these measurements might have systematic differences, and a complete discussion of the differences is beyond the scope of this paper. The baseline comparison simply shows how much two independent measurements of the velocity might differ and still be useful measures.

The statistical comparisons of both the MCC and the inverse solutions with the drifter and ADCP vectors are shown in Table 2. The number of drifter comparison vectors for each 12-hour period was about 35-40; the number of comparison vectors for ADCP is shown for each solution in Table 2. There are several clear trends in Table 2, of which the most apparent is the similarity between the statistics of the MCC and the inverse solutions. Based on the ADCP comparisons, on average the MCC estimates have slightly larger magnitudes, an rms ratio of 0.58 for all the estimates,

compared with 0.51 for the inverse solutions, but at the expense of the directional disagreement, an rms difference of 74° compared with 66° for the inverse solutions. However, because the number of estimates is small and the scatter in the measures in Table 2 is large, these differences are not statistically significant. These differences between AVHRR and in situ data translate into rms differences in vector velocities of about 0.2-0.4 m s⁻¹ in a region containing a jet with velocities of approximately 1.0 m s⁻¹.

Some other trends can be seen in Table 2 by comparing the differences in the statistics for ADCP with the differences for the drifters, recalling that the drifters preferentially sampled the jets. Using the rms ratio for all the AVHRR-derived velocity estimates in Table 2 (0.34 for drifters and 0.55 for ADCP) and taking into account the 10% reduction for interpolation, the AVHRR methods underestimate the drifter speeds by about 56%. This compares with an underestimate of the drifter speeds using ADCP of about 22%. The AVHRR methods underestimate speeds for the ADCP by about 35%. The rms directional difference relative to the drifters is about 60°, which is essentially the same as that for interpolated ADCP data (59°). The rms directional difference for all AVHRR-derived estimates for the ADCP is slightly larger (70°) than that for the drifters. This rms directional difference consists of both a mean difference and a standard deviation; the mean angular difference ranged from 0° to 29° for the estimates in Table 2. The MCC estimates had relatively small mean differences relative to the drifters (that is, in the jets) and larger mean differences relative to the ADCP, whereas the converse was true for the inverse solutions: the larger mean angular differences (9°-21°) were relative to the drifter data. For a baseline comparison, the mean angular difference between the drifter and ADCP vectors was 4°. There was no distinguishable pattern in the sign of the mean angular difference.

All five estimates from each method were compared with the Geosat cross-track velocity from day 200, which was the nearest measurement in time. This Geosat profile crossed the eastward flowing jet at nearly right angles, thus giving a reasonable estimate of the maximum jet speed. For these scalar comparisons the velocity vectors were interpolated to points along the Geosat subtrack, with a resolution of about 7 km, and the cross-track component at every point was computed. Then a linear regression was calculated between

TABLE 2. Comparison of Solutions With Drifter and ADCP Vectors

Solution	Time	Drifter		ADCP		
		$\delta\theta$	Ratio	$\delta\theta$	Ratio	No.
MCC	198.75	70°	0.27	81°	0.46	13
MCC	199.25	63°	0.26	63°	0.48	21
MCC	199.75	55°	0.38	65°	0.54	17
MCC	200.25	57°	0.41	86°	0.74	18
MCC	200.75	49°	0.46	72°	0.65	11
Inverse	198.75	49°	0.25	50°	0.48	11
Inverse	199.25	73°	0.25	53°	0.47	21
Inverse	199.75	68°	0.40	71°	0.62	17
Inverse	200.25	62°	0.33	53°	0.46	18
Inverse	200.75	52°	0.29	92°	0.48	13
Combined	199.75	39°	0.35	71°	0.55	16

the velocity estimate \hat{u} and the Geosat geostrophic velocity u_g ,

$$\hat{u} = au_g + b \quad (5)$$

with all velocities given in meters per second. The results are shown in Table 3, which includes the squared correlation coefficient, ρ^2 . Again the results for the MCC and inverse solutions are similar, with magnitudes (rms value for a) of 0.56 and 0.44, respectively. Although the altimeter measures objectively, the jet represented a large part of the Geosat velocity variance in this particular profile. Thus the Geosat comparison data represent a sampling situation somewhere between that of the preferential jet sampling of the drifters and the more objective ADCP sampling. The resulting underestimates of 34% (MCC) or 46% (inverse) are therefore consistent with the vector data comparisons.

The correlation coefficients in these comparisons (Table 3) are relatively high (rms value for ρ^2 is 0.58), suggesting that, ignoring the low jet speeds, the flow fields from the AVHRR images are qualitatively accurate. This is illustrated in Figure 6, which shows the Geosat profile (solid line) on day 200 along with the profiles for the third and fourth estimates for both the MCC and inverse methods. Note that the resolution of flow features near the ends of the profiles is somewhat better using the inverse method than using the MCC method. Away from the edges of the images, multiple peaks of onshore and offshore flow are well resolved by both methods, which suggests that the underestimate of the jet speeds is not due to inadequate spatial resolution in the estimates. Correlation coefficients were substantially lower for regressions with the Geosat data from day 203 along a subtrack which is closer to the coast and which had a larger temporal separation. For the MCC estimates these correlations (ρ^2) were 0.34–0.56, and for the inverse solutions these correlations were much lower, 0.03–0.36. Correlations with the Geosat data for day 197 were even smaller, suggesting that the velocity field was changing too fast for these data to be useful for comparisons.

Comparison of AVHRR Estimates

To determine whether the AVHRR solutions agreed more with each other than with the data, we directly compared the two AVHRR-derived fields both quantitatively and qualitatively. The results using the vector statistical measures are shown in Table 4. The rms ratio of the magnitudes

(inverse/MCC) has a mean of 0.66 over the five intervals; thus the inverse solutions have magnitudes one-third less than the MCC estimates. This is apparently because the inverse solutions are smoother than the MCC estimates: after smoothing with the objective analysis procedure described in the next section, the MCC jet magnitudes were quite similar to those of the inverse solution (compare Figures 4d, 5a and 7a). The difference in direction between the MCC and inverse solutions ranges from 60° to 75°, values comparable to the differences between either AVHRR solution and the ADCP vectors. Thus, although Table 2 suggests that the AVHRR solutions have similar directional differences with the data, they differ in direction as much from each other as either does from the data.

Nevertheless, a qualitative comparison of the solutions (Figures 4d and 5a) shows most of the same features in the circulation pattern. A jet flows toward the southwest from the northern edge (39°N, 125°W) to the western edge of the domain near 36.5°N, 128°W, then flows toward the southeast near 36°N, 126°W. A cyclonic eddy is found inshore of the jet near 37°N, 126.5°W. Anticyclonic eddies are found northwest of the jet near 38.5°N, 126.5°W, and inshore of the jet near 35.5°N, 124°W. The MCC method results in a more continuous, meandering jet, whereas the inversion of the heat equation depicts the southern half of the jet as the inshore part of an anticyclonic eddy at 35.5°N, 126°W, that is shown only weakly, if at all, in the MCC solution. In general, the inverse solution is more eddylike and the MCC estimate is more jetlike. The difference in character of the estimates is probably a function of the finer spatial grid of the inverse solution (18 km versus 27 km for the MCC), which allows for smaller features, and the minimization of horizontal divergence, which tends to produce closed circulation patterns.

The inverse solution shows an onshore and northward return flow southeast of the northern half of the jet, stretching from 36.5°N, 126°W to 38°N, 124°W. This coherent onshore flow is missing in the mean MCC estimate between 124°W and 126°W (Figure 4d), although it is present in a noisy fashion on some of the individual MCC fields (Figure 4c) and it appears in the subjective flow vectors shown in Figure 12 of Strub *et al.* [1991]. ADCP vectors at 37.5°N, 124.5°W (Figure 3) and dynamic height fields from the complete July 13–18 survey [Huyer *et al.*, 1991] support the presence of a band of onshore flow more like the inverse solution than the MCC estimate. Just south of this region, at about 37.3°N,

TABLE 3. Comparison of Solutions With Geosat Cross-Track Velocity

Solution	Time	a	b	ρ^2
MCC	198.75	0.56	0.07	0.43
MCC	199.25	0.42	-0.03	0.53
MCC	199.75	0.64	-0.01	0.53
MCC	200.25	0.57	-0.07	0.69
MCC	200.75	0.58	-0.01	0.74
Inverse	198.75	0.39	-0.08	0.49
Inverse	199.25	0.49	-0.09	0.72
Inverse	199.75	0.48	-0.01	0.60
Inverse	200.25	0.49	-0.05	0.38
Inverse	200.75	0.33	-0.02	0.54
Combined	199.75	0.63	-0.05	0.58

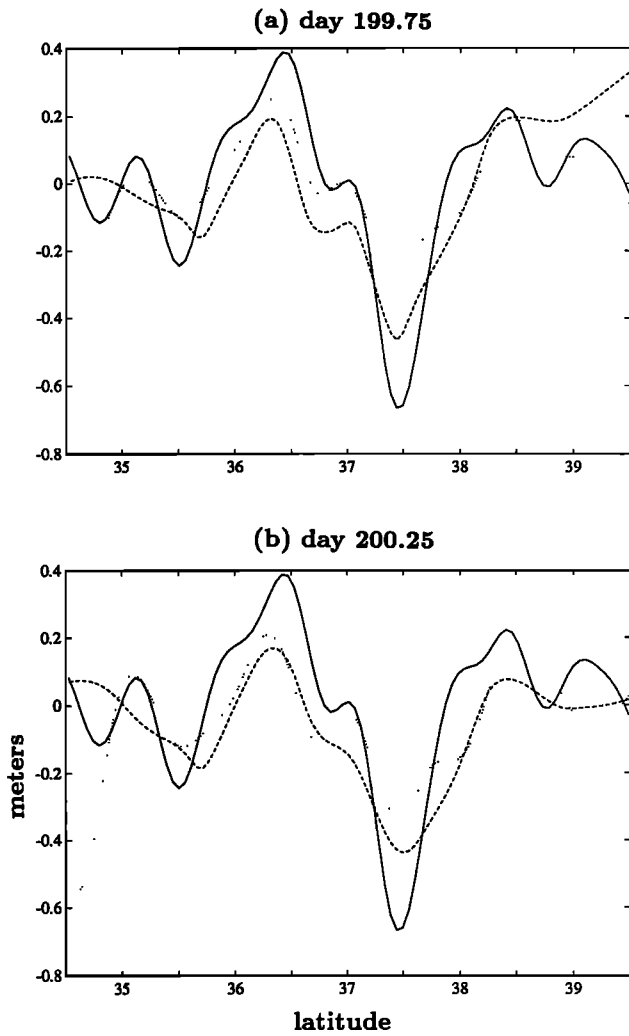


Fig. 6. The cross-track velocity profiles for Geosat and both types of AVHRR estimates. The Geosat geostrophic velocity profile for day 200 (solid line) and the MCC (dashed) and the heat equation (dotted) solutions are shown for (a) day 199.75 and (b) day 200.25. Both solutions underestimate the magnitudes of the velocity, especially that of the offshore jet at about 37.5°N. However, both solutions resolve most features in the flow field as quantified by the relatively high correlations between the profiles (see Table 3).

TABLE 4. Comparison of MCC and Inverse Solutions

Time	$\delta\theta$	Ratio*
198.75	75°	0.63
199.25	68°	0.69
199.75	60°	0.76
200.25	61°	0.69
200.75	65°	0.58

*Inverse/MCC

124.5°W, along the cold filament extending southwest from Point Reyes, the estimates also disagree. The MCC estimate suggests offshore flow, whereas the inverse solution suggests onshore flow. A few days later (day 203), the Geosat profiles (Figure 2) suggest pronounced offshore flow just south of this region at about 36.8°N, 124.5°W.

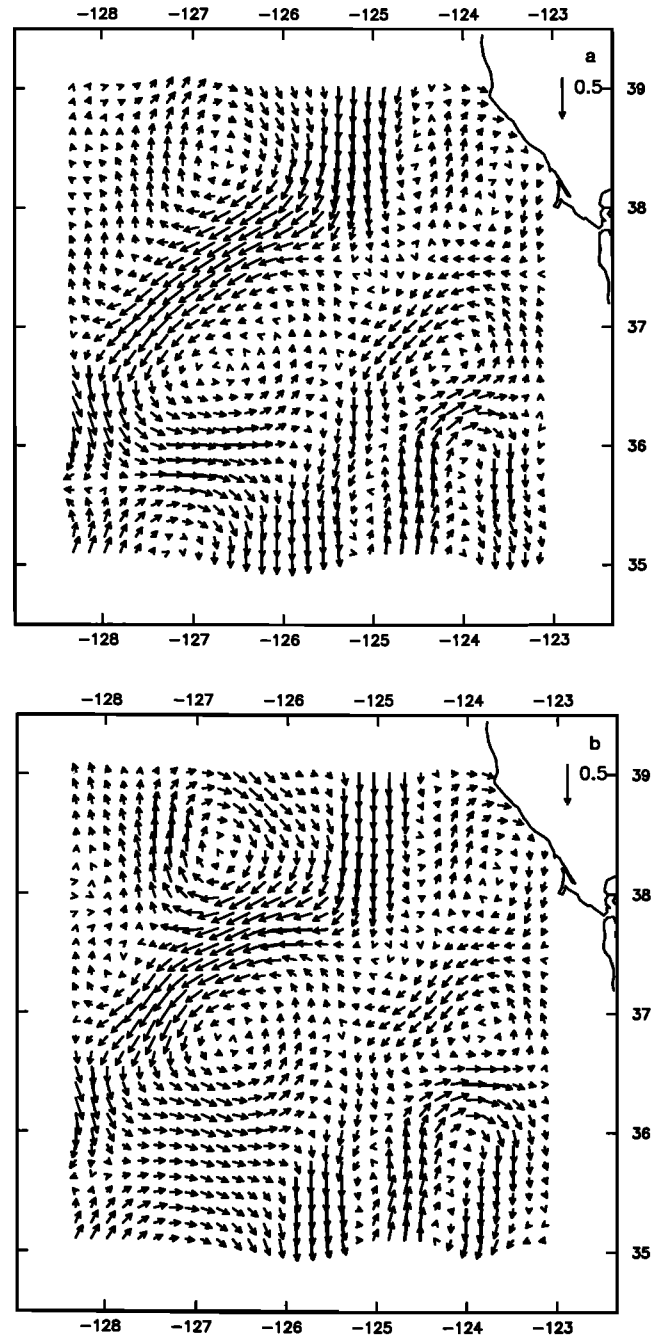


Fig. 7. The velocity field reconstructed from the stream function using objective analysis of the field shown in Figure 4d. (a) for the MCC vectors alone and (b) including the altimeter velocities along tracks for days 197, 200, and 203.

Combining Information

To test whether either AVHRR method could be combined with other data to obtain better estimates, we used two basic techniques. The first was the addition of a constraint on the heat equation inverse to require the solution to match other data. The second method was objective analysis to combine MCC vectors with in situ data. The determination of whether the combined solutions were better than the original AVHRR solutions was limited by the accuracy of the comparison data, because the angular differences between the drifter and ADCP vectors were as large as those

between the AVHRR and either in situ data set. Nevertheless, an increase in the magnitudes of the AVHRR velocities with no degradation of the angular differences would clearly represent an improved solution.

Combined inversions. The heat equation inversion is a least squares procedure which can be augmented with additional constraints by simply adding more equations (rows) to the system, with a weight which reflects the importance of the new information. To the system given by (3) and (4) we added the requirement that the velocity solutions (u, v) match the specified vectors (u_s, v_s) at the locations x_i , that is,

$$\beta[u(\vec{x}_i) = u_s(\vec{x}_i)] \quad (6)$$

$$\beta[v(\vec{x}_i) = v_s(\vec{x}_i)] \quad (7)$$

where β is the weight given to this constraint relative to (4), analogous to α in (3). The specified vectors in this case were from the MCC estimates. Since the cross-correlation coefficient r from the MCC method reflects the accuracy of the velocity estimate at that point [Tokmakian *et al.*, 1990], a multiple of the correlation value was used as the weight in (6) and (7), i.e., $\beta = r\beta_0$.

With the additional rows the matrices to be factored for the inverse were substantially larger; therefore the combined inversions were computed at a somewhat reduced resolution (54 km) compared with the original inversions (35 km), which corresponded to $nd = 3$ instead of $nd = 2$, as defined in Appendix C. A control solution at the lower resolution using only the AVHRR data for day 199.75 is shown in Figure 5b and its comparisons with vector data are shown as the "no data" solution in Table 5. This solution had the same input information as in Figure 5a, but the weight α was decreased slightly to maintain approximately the same speeds in the solution: a magnitude ratio of 0.57 for ADCP compared with 0.62 and a slight increase in the directional difference, 77° compared with 71° . Some features were lost in reducing the spatial resolution, the most notable of which is the breaking up of the continuous band of onshore flow south of the jet at 37.5°N , 125°W into two cyclonic eddies.

For the third time interval (day 199.75), the inverse solution was constrained to match the MCC estimates (Figure 5c); this solution differed from the ADCP data by as much as either of the estimates alone (solution Combined in Table 2), although there was a significant decrease in the directional difference relative to the drifters (from 57° to 39°). The comparisons with Geosat data showed no signifi-

cant improvement over either estimate alone, with $a = 0.63$ and $\rho^2 = 0.58$ (solution Combined in Table 3). Thus there was no obvious gain in information from the combination of the two methods.

We next tested whether the inversion of the heat equation could be improved by the addition of altimeter data. Because real velocity vectors are often approximately parallel to the isotherms and therefore produce little or no change in SST, the magnitude of the velocity could be largely underestimated in the heat equation inversion [Kelly, 1989]. The altimeter gives an estimate of the component of the geostrophic velocity perpendicular to the subtrack, so that except where the satellite subtrack is nearly parallel to the isotherms, the cross-track velocity component should improve the velocity estimate. The addition of altimeter data into the inversion was analogous to the MCC assimilation, except that only one velocity component could be matched to the altimeter data. The component of the solution vector (u, v) in the cross-track direction was required to match the geostrophic velocity from the altimeter u_g , that is,

$$\gamma(u \cos \Psi + v \sin \Psi = u_g) \quad (8)$$

where Ψ is the angle between the x axis of the images (here, due east) and the perpendicular to the satellite subtrack. Again both sides of (8) were weighted relative to the heat equation, by the factor γ .

We assimilated a single altimeter profile for day 200 into the solution for day 199.75 and we assimilated profiles for both days 200 and 203, using $\gamma = 0.2$ in all cases. The solution using both profiles is shown in Figure 5d. The control case for the altimeter assimilations was the inversion at the lower spatial resolution (Figure 5b). The single-profile assimilation did not significantly improve the solution (Table 5); however assimilation of both profiles (Figure 5d) gave increases in the ratios which were marginally significant, without increasing the directional differences. The assimilation degraded the fit to the heat equation from a misfit of about 64% for the control case to misfits of 69% for one profile and 74% for two profiles. The assimilation of the Geosat data also changed the character of the velocity solution near the subtracks (compare Figures 5b and 5d). It increased the strength of two anticyclonic eddies, one north of the jet at about 38°N , 126°W and one south of the jet at about 36°N , 124°W . It also created offshore flow near 36.5°N , 124.5°W , more like the MCC estimate (Figure 4d). The offshore flow was apparent in the original inversion (Figure 5a) but disappeared with the reduction in resolution (Figure 5b).

TABLE 5. Geosat Assimilation Compared with Drifter and ADCP Vectors

Solution	Drifter		ADCP		
	$\delta\theta$	Ratio	$\delta\theta$	Ratio	No.
Inverse					
No data	57°	0.34	77°	0.57	18
Day 200	58°	0.39	85°	0.59	18
Both days	56°	0.38	69°	0.61	17
MCC					
No data	48°	0.26	55°	0.48	18
Both days	67°	0.27	58°	0.50	18

Objective analysis. To smooth the MCC vectors and combine them with altimeter data, we used objective analysis (OA) [Bretherton *et al.*, 1976]. We first fit a stream function to the MCC vectors using OA and then calculated a new vector field from this stream function, which had, by definition, zero divergence. We used the isotropic covariance function chosen by Walstad *et al.* [1991] for the stream function, based on an analysis of ADCP data in the CTZ region:

$$C_{\psi\psi} = \left(1 - \frac{s^2}{d^2}\right) e^{-(s/c)^2} \quad (9)$$

where $C_{\psi\psi}$ is the covariance function of the stream function field, ψ is the stream function, s is the distance to data points, and c and d are length scales with values $c = 100$ km and $d = 120$ km. Walstad *et al.* used smaller length scale values of $c = 50$ km and $d = 60$ km; the larger values used here were necessary to accommodate the larger spacing of the altimeter tracks. A rough estimate of the uncertainties in the MCC velocities, with units of meters per second, was taken to be $(1 - r)$, where r is the correlation coefficient. An estimate of 0.1 m s^{-1} was used for the uncertainty in the altimeter velocities.

Velocity estimates were reconstructed from the vectors shown in Figure 4d using OA without (Figure 7a) and with (Figure 7b) altimeter data. Both the smoothing of the objective analysis and the incorporation of altimeter data affected the statistics of the velocity estimates relative to the in situ data. The smoothing alone reduced the rms angular differences (compare Tables 2 and 5) from 55° to 48° for the drifters and from 65° to 55° for the ADCP vectors (a significant improvement). However, the magnitude ratios also decreased significantly, from 0.38 to 0.26 and from 0.54 and 0.48 for drifters and ADCP, respectively. The addition of the Geosat data had little effect on the magnitudes (Table 5), but it did increase the rms angular differences for the drifters from 48° to 67° , which was a significant degradation. Thus the assimilation of Geosat data into the MCC method did not improve the estimate statistics. Qualitatively, the velocity fields in Figure 7 contain the same features as previously seen, with the overall impression of a strong jet, meandering through a field of cyclonic and anticyclonic eddies. Inclusion of the altimeter data in the OA appears to have both increased the flow around the closed eddies and increased the continuity within the meandering jet.

5. DISCUSSION

How good are the AVHRR methods for estimating velocity? Both methods produce nearly instantaneous pictures of the energetic flow features, which agree qualitatively with other velocities on scales greater than 50–100 km. Both methods systematically underestimate the magnitudes of the velocities as measured by drifters and ADCP at 20 m depth; however, the directional differences are comparable with those obtained by comparing ADCP vectors with drifters for the same period. We suspect that the underestimate of the velocity, particularly in the jets, is inherent in the AVHRR data, rather than a limitation of the methods. We do not believe it is due to inadequate spatial resolution because a comparison with the Geosat velocity profiles (Figure 6) shows that all the small-scale features of the flow field are present in both AVHRR estimates. With compara-

ble spatial resolution (the half-power point for the low-pass filter was 55 km) the Geosat profiles have jet velocities 1.5–2 times larger than the AVHRR estimates. Note that the average spline knot spacing for the inverse solution was about 35 km and the correlation tile for the MCC method was about 27 km. Varying the constraint weighting factors in the inversions did not produce more energetic jets in the solutions: the more energetic solutions had large vectors in a few regions near the edges of the images, with correspondingly large divergences, rather than larger jet speeds.

A detailed comparison of drifter displacements and SST feature motion in the region of the jet confirmed that the drifters are moving faster. For a small subsample of initial drifter locations, features were tracked subjectively and by the MCC method. The average ratio of subjectively determined velocity magnitudes to drifter magnitudes was approximately 0.6, while the MCC method yielded an average ratio of 0.4. Thus, subjectively tracking features produces somewhat greater velocities than the automated feature tracking (MCC) but does not produce the large velocities of the drifters. Some drifters moved across the cold filament, leaving SST features behind and moving into warmer water with relatively no features. In some regions, it was impossible to track features at all, even when strong velocities were indicated by the drifters (38.8°N , 123.9°W , in Figure 1). This illustrates the fact that in some regions, processes other than horizontal advection dominate the heat budget and make the major contribution to changes in the SST field, violating the assumptions inherent in both AVHRR methods.

The similarity in the estimates from the two methods and in the nature of the errors suggests that the methods are equivalent, i.e., the small-scale features which are cross correlated in the MCC method must be the same features which produce the SST differences used by the inversion to estimate velocities. The underestimate of the jet velocity suggests that either the small-scale SST features do not move at the speed of a water parcel in the jet or that the core of the jet is isothermal and therefore there is no SST difference resulting from advection in the jet core.

To some extent the problems of the AVHRR estimates may be corrected by assimilation of other data, although the preliminary attempts described here showed only modest improvements, and only for the heat equation inversion. The results here are somewhat in contradiction with the results of Taggart [1991], who used this same method of assimilation with synthetic altimeter data. Using some of the same AVHRR images (A, C, E, and G in Table 1) and profiles constructed from the ADCP vectors, Taggart showed that assimilating profiles at 25-km spacing gave little improvement in the velocity solutions over assimilation of a single profile. The analyses here suggested that two profiles, separated by about 100 km, gave better results than a single profile. Clearly the problem of combining AVHRR with other data needs a more careful examination.

What are the advantages and disadvantages of each AVHRR method? The inversion of the heat equation works better with slightly longer time separation between images (6–18 hours) and does not require the full spatial resolution of the images. Tests with these same images decimated by a factor of 4 produced similar statistics to the 1-km resolution images, suggesting that the inversion should work on the Global Area Coverage (GAC) 4-km data that are rou-

tinely archived, if adequate cloud flagging can be done. On the other hand, the MCC method gives larger jet velocities. The shorter optimal temporal separation of the MCC method would be an advantage when a region was clear only for a short period because of cloud cover. The MCC method may also be more successful when SST gradients are weak or when the SST gradients cannot be corrected properly.

To what extent is the divergence field of the AVHRR-derived estimates realistic and informative? The horizontal divergence was calculated from an average of the estimates for the last two 12-hour periods (days 199.75 and 200.25) for both the MCC and inverse methods, because divergence fields for individual estimates were quite noisy. The divergence field from the MCC method (not shown) had maximum magnitudes of 0.4–0.6 days⁻¹ ($5\text{--}7 \times 10^{-6} \text{ s}^{-1}$); and these maxima occurred both within and outside of the region of strong offshore flow. Unlike the MCC estimate, the field of divergence from the inversion of the heat equation has its maximum values (about 0.4 days⁻¹) concentrated near the jet or near the coast. Much of the jet was convergent, with a maximum in the cyclonic eddy at its offshore edge (Figure 5a) and near where this eddy appears to be pinching off at 37.5°N, 125°W. This pattern of convergence was similar to the patterns of downwelling seen in the numerical simulation of a jet by *Haidvogel et al.* [1991, Plate 2]. An evaluation of the usefulness of the divergence field is limited by the lack of comparison data; the field from the inverse solution has plausible structure and magnitudes.

What information can be gained from the AVHRR-derived velocities? The qualitative agreement between the AVHRR estimates and the in situ data suggests that they can be useful in determining the appropriate conceptual model of the jets [see *Strub et al.*, 1991]. In all AVHRR estimates the offshore-directed jet is fed by flow from the north; there is no evidence of flow from the south being directed into the jet, except where the cyclonic eddy near its offshore edge recirculates water from the jet. In all AVHRR estimates the offshore-directed jet has a strong return flow; the return flow bifurcates into a cyclonic eddy and a southward flow similar to the mean 1988 flows calculated from the drifters [*Brink et al.*, 1991, Figure 3d]. This asymmetry of the jet (inflow from the north and outflow to the south) suggests that the jets are primarily meanders of the southward flow, not simply an illusion created by the alignment of the nearby eddies.

Nevertheless, this meander is embedded in a strong eddy field and it is probably affected by interactions with these eddies. The anticyclonic eddy to the northwest of the jet is a feature that was observed only in the AVHRR-derived fields, despite the fact that it corresponds to a region of small SST gradients. An eddy has been found in this location during a number of summer surveys [*Rienecker et al.*, 1987] and there has been speculation that this eddy was present during the 1988 surveys [*Lagerloef*, 1992], although none of the drifters entered this eddy. The field survey on July 13–18 [*Huyer et al.*, 1991] shows what could be the eastern part of this eddy but did not sample far enough west to resolve more of it; the field survey on June 20–27 shows perhaps half of an eddy, in the same approximate location but again did not sample far enough west to determine whether it was a closed eddy. Both AVHRR methods resolve this eddy, and its existence is supported by an onshore flow north of the jet in the Geosat data on day 200 (Figure 2). This anticyclonic eddy and the

cyclonic eddy to its south, which is the offshore end of the jet, have a dipole structure similar to that in the detached eddy in the numerical simulations of *Haidvogel et al.* [1991]; in fact, the narrowness of the jet and the onshore flow at 37.5°N, 125°W (compare Figure 5a and Figure 3) suggest that the meander may be pinching off this pair of eddies.

6. SUMMARY AND CONCLUSIONS

A set of 11 relatively cloud-free AVHRR images from a 3-day period and coincident drifter, ADCP, and altimeter data were used to evaluate the performance of two methods of estimating horizontal velocities in the upper ocean from sequences of AVHRR images. The two methods are the MCC method [*Emery et al.*, 1986] and the inversion of the heat equation [*Kelly*, 1989]. The comparisons of the estimates with the data were given in terms of the rms angular differences and the rms ratio of the magnitudes.

The most striking result is the similarity between the comparison statistics of the MCC and the inverse solutions and the qualitative agreement between the estimates. Both methods underestimate the magnitudes of the ADCP vectors by about 35% and the drifters by about 56%. Root-mean-square differences in direction were 60°–70°, which were only slightly larger than that from a baseline comparison (59°) established by interpolating ADCP vectors to the positions of velocity vectors from drifters. We suggest that the methods are equivalent, i.e., the small-scale features which are cross correlated in the MCC method must be the same features which produce the SST differences used by the inversion to estimate velocities.

The underestimate of the velocity, particularly in the jets, is inherent in the assumptions used to derive the velocity from the AVHRR data, rather than a limitation of a particular method. The small-scale SST features near the jet move more slowly than a water parcel. In addition, the core of the jet is nearly isothermal so that advection produces little SST difference between images. The underestimate of the jet speeds is not due to inadequate spatial resolution in the estimates. Both methods resolve the energetic flow features with horizontal scales of 50 km or more, although the inverse method appears to resolve flow features better near the edge of the images than the MCC method. Nevertheless the Geosat geostrophic jet velocities with comparable spatial resolution are 50–100% larger than the AVHRR estimates.

Despite their similar comparison statistics, the AVHRR-derived fields from the two different methods differed from each other in the statistical characterization nearly as much as they differed from the in situ data. The MCC estimates had larger magnitudes (by about one third) than the inverse solutions, particularly in the jets, while the inversion produced smoother fields. The inversion uses slightly longer periods between images (12–18 hours compared with 4–12 hours for the MCC method) and perhaps lower spatial resolution (4 km compared with 1 km), making use of archived GAC data possible. It has the disadvantage of requiring an atmospheric correction for temperature gradients. Both methods require that as many images as possible be collected over periods of a few days. Both methods would also benefit from automated cloud screening techniques.

The AVHRR methods were combined with each other and with altimeter data to attempt to improve the estimates. The combination of the two methods did not significantly

improve the statistical comparisons with the in situ data. Assimilation of the altimeter data into the inversion gave a modest improvement in the comparison statistics when data from two subtracks were used. The large angular differences in the baseline comparison between the drifter and ADCP vectors and the small spatial region covered by the in situ data made it difficult to establish whether incorporating altimeter data significantly improved the solutions. Although the assimilation of altimeter data clearly needs to be investigated further, these results suggest that multiple altimeters (ERS-1 and TOPEX/Poseidon) or aircraft-deployed drifter data should be useful in constraining the AVHRR-derived fields.

The qualitative accuracy of the flow fields suggested an interpretation of the velocity estimates in terms of proposed conceptual models of the California Current. The jets appear to be meanders of the southward flow and indicate a strong return flow south of the offshore-directed flow near Point Arena. These meanders are clearly interacting with a strong eddy field; an anticyclonic eddy to the northwest of the jet was a robust feature of all the AVHRR-derived fields and its existence was supported by an onshore flow north of the jet in the Geosat data. The divergence fields derived from the velocity estimates were noisy and therefore somewhat suspect; however the field computed from the inversion showed the jet to be predominantly convergent.

APPENDIX A: PATH LENGTH CORRECTION FOR AVHRR IMAGES

As discussed by *Kelly and Davis* [1986] (hereinafter KD) an effective empirical correction for water vapor errors in the SST maps for northern California summer can be made by assuming that atmospheric water vapor is constant over several days. Therefore the correction can be parameterized simply in terms of the path length between the satellite and the sea surface or, alternatively, as a function of the zenith or nadir angle, θ [cf. KD]. Zenith angles for the center of the images were estimated from maps of the orbital subtrack.

The relationship between the actual sea surface temperature T_s and the brightness temperature T_λ for a single channel of the AVHRR can be written [cf. KD]

$$T'_\lambda = T'_s - (\rho_0 + \alpha U)(q_0 + q_1 T'_s) + \alpha F(p_0 + p_1 T'_s) \quad (A1)$$

where $T'_\lambda = T_\lambda - T_0$, $T'_s = T_s - T_0$, and T_0 is a reference temperature close to the mean SST in the maps. The factor ρ_0 is the reflectance of the sea surface at zero zenith angle, and α is the ratio of the actual path length to the path length at zero zenith angle, which for small angles can be approximated as $1/\cos\theta$. The terms U and F represent the absorption and emission, respectively, of infrared radiation by the atmosphere. The terms q and p come from a Taylor expansion of the inverse of the Planck function around the reference temperature T_0 , i.e., $q = P/P'$ and $p = 1/P'$, where the Planck function relates the infrared radiance L_λ to the temperature of the radiator, $L_\lambda = P_\lambda(T)$, and $P' = \partial P/\partial T$. Here q_0 and p_0 are the functions q and p evaluated at T_0 and q_1 and p_1 are the partial derivatives of q and p with respect to temperature, respectively, also evaluated at T_0 .

An empirical correction for the channel 4 brightness temperatures was found by computing the linear regression coefficients between the spatial mean and standard deviation of the brightness temperature T_λ for each image and the path length ratio α (see Table A1). These relationships can be seen by rewriting (A1) as

$$T'_\lambda = T'_s(1 - \alpha A) - \alpha B - C \quad (A2)$$

where

$$A = q_1 U - p_1 F \quad (A3)$$

$$B = q_0 U - p_0 F \quad (A4)$$

$$C = \rho_0 q_0 \quad (A5)$$

The quantity ρ_0 was assumed to be -0.01 , based on KD (note that there was a sign error for this quantity in KD); its value does not affect the inversions because it is a constant for all the images and the SST maps are always differenced. The standard deviation of the brightness temperature σ_λ is then related to the standard deviation of the actual SST, σ_s , by

$$\sigma_\lambda = (1 - \alpha A)\sigma_s \quad (A6)$$

The quantities σ_s and A were found from the linear regression between the standard deviation of the images and α , and then this value of A was used to determine the value of

TABLE A1. SST Before and After Path Length Corrections

Image	Zenith Angle	Before		After	
		Mean T_λ	s.d.	Mean T_λ	s.d.
B	46°	14.71	0.915	16.20	0.997
C	3°	15.23	1.166	16.06	1.260
D	26°	15.11	1.097	16.10	1.174
E*	45°	—	—	16.13	1.262
F	49°	14.59	1.336	16.20	1.513
G	18°	15.12	1.290	16.02	1.396
H	47°	14.48	1.042	15.98	1.102
I	52°	14.08	1.023	15.74	1.103
J	29°	14.91	1.129	15.94	1.242
K	30°	15.21	0.808	16.28	0.870

*Image E was not used to compute the empirical correction.

B in the linear regression between the mean image temperature perturbation $\langle T'_\lambda \rangle$ and α . These relationships can be seen most clearly by rearranging the terms in (A2) and averaging the temperatures spatially, to get

$$\langle T'_\lambda \rangle = \langle T'_s \rangle - C - \alpha(A \langle T'_s \rangle + B) \quad (\text{A7})$$

The spatial average of T'_s , which was assumed constant for the series of images, was also found. The regressions were computed on a common 256×256 pixel subset of the original 512×512 images to eliminate possible contamination by unmasked land pixels, clouds, and fog. The resulting values for $\langle T'_s \rangle$ and σ_s were 2.13°C and 1.20°C , based on a reference temperature of 14°C . The values of A and B were then used along with (A3) and (A4) to estimate values of the parameters U and F , which were 0.0822 and 0.477×10^{-6} . There was considerable scatter in the regression of the standard deviation of temperature against path length, which reflects the inaccuracy of the assumption of constant water vapor. Nevertheless, the values of U and F compare favorably with those obtained by KD, which were 0.123 and 0.643×10^{-6} respectively, and suggest somewhat less atmospheric water vapor in July 1988 than in July 1981.

APPENDIX B: DETAILS OF THE MCC CALCULATIONS

A number of trade-offs affect the choice of the sizes for the correlation tile and the search window, as well as the use of the high-pass filter. To resolve the motion in narrow jets, small correlation tiles are desired. However, larger correlation tiles contain more distinctive features and therefore give more degrees of freedom in the correlations. If the search window is large, as is required by long periods between images and large velocities, a greater number of cross correlations must be calculated, increasing the chance of spurious cross correlation coefficients and increasing the computation time. If the search window is kept artificially small, the ability to find realistic maximum velocities is lost. In the present study, the search window was large enough (10–30 pixels, depending on separation times) to find maximum velocities of slightly over 1.0 m s^{-1} . In retrospect, no coherent velocities over 0.8 m s^{-1} were found, implying that a smaller search window could have been used. The size of the correlation tile used was a 25-pixel square, small enough to marginally resolve jets of 20–40 km width, and large enough to contain a number of distinctive features with scales of 5–10 km.

The tendency for cross-correlation calculations to be dominated by larger-scale features in the fields can be reduced by high-pass (in wavenumber) filtering the images or by calculating SST gradients. Calculating gradients on the smallest possible grid (centered differences with 2-pixel spacing) allows very precise calculations of displacements in the absence of rotation or distortion. This method has been used with success in tracking ice motion [Collins and Emery, 1988]. The large degree of distortion or rotation in oceanic features between images, however, results in very low cross correlations between gradient images. Therefore we used a high-pass filter (two-dimensional cosine filter with a wavelength of 30 km) on the images, which retained features with scales less than 20–25 km.

An empirical estimate of the significance level of the maximum cross correlation was determined by applying the

MCC method to filtered images separated by 11 days, which should have produced only random cross correlations. For a search window that allowed 10-pixel displacements in all directions, only approximately 10% of the maximum cross correlations were above 0.4. For a search window that allowed 20- and 30-pixel displacements, approximately 10% of the maximum cross-correlations were above 0.55 and 0.60, respectively. These values are used as approximate 90% confidence limits for r . When no high-pass filter was applied to the images, these values were much higher (0.65, 0.79, and 0.85, respectively).

There are a variety of search strategies which can be employed in finding the location of the maximum value of r . The brute force method moves the correlation tile pixel-by-pixel through the search window, calculating r at each location and choosing the absolute maximum. Although this was the method employed in the present study, nearly identical results were obtained in much less time by first using a coarser grid to search for the approximate locations of all of the local maxima within the search window. The location of each local maximum was then used as the starting point of a new calculation, using the full resolution data set, marching up the gradient in r until a new local maximum was found. The location of the largest value of r calculated within the search window was chosen as the location of the displacement. By skipping to every third pixel before calculating the initial cross correlations and using only every other pixel in the initial cross-correlation calculations, the speed of the computation was increased by a factor of 8. Combined with the increased speed of modern workstations, this method produces velocity calculations with 20-km resolution (441 vectors) for a 512×512 pixel image pair in 6–10 min (on a VAXstation 3100), compared to the 18–24 hours required previously using the brute force method (on a microVAX II).

A final aspect of the search strategy involves the inclusion of rotation. Besides simply displacing the initial search tile and calculating r , the initial tile can be rotated through a reasonable range of angles to accommodate rotation of the features [Kamachi, 1989; Tokmakian *et al.*, 1990]. Previously, the computation time for these additional calculations was prohibitive. Although it is now feasible, the additional searches increase the chance of erroneous high correlations. Our computations showed that with images close enough together in time, curving jets and eddies with diameters less than 100 km can be resolved with the basic method, that is, without rotation. Emery *et al.* [1992] in their investigation of an alternative method of following rotation in closed rings and eddies, also noted that the basic method, without rotation, produces similar results.

APPENDIX C: DETAILS OF THE INVERSE CALCULATIONS

Several specific changes from Kelly [1989] were made in the inversion method used here. The two-dimensional Fourier series used as basis functions were replaced by two-dimensional biharmonic splines (see, for example, Sandwell [1987]). The two-dimensional biharmonic spline Green's function $\phi(\vec{x})$ is $|\vec{x}|^2(\ln|\vec{x}| - 1)$. The two horizontal velocity components are expanded in the Green's functions as

$$u(\vec{x}) = \sum_{j=1}^M A_j \phi(\vec{x} - \vec{x}_j) \quad (\text{C1})$$

$$v(\vec{x}) = \sum_{j=1}^M B_j \phi(\vec{x} - \vec{x}_j) \quad (C2)$$

where the summation is over M valid subsets with centers \vec{x}_j in the spatial domain of the image pairs. The spatial resolution of the splines depends on a parameter, called nd here, which sets the number of data per knot in the spline. The larger the value of nd , the smoother the velocity solution. The number M of coefficients A_j or B_j (which is the number of knots in the spline) is the total number of subsets in the images divided by the square of nd . In these calculations there were 29 subsets in the x direction and 32 subsets in the y direction, so that the number of coefficients was $(29/nd) \times (32/nd)$ or 224 for $nd = 2$. We used a value of 2 or 3 for nd in all of the inversions, which gave a spatial resolution of about 35 or 53 km, respectively.

The use of biharmonic splines allowed us to use a simpler set of constraints on the velocity field. Test inversions on the images minimizing divergence, kinetic energy, and relative vorticity showed that minimizing divergence was the most effective in producing solutions which resembled the in situ data. The global kinetic energy constraint used by Kelly [1989] was replaced here by a constraint applied only in regions of missing data. If only one image of a pair was cloud-free on a given subset, so that the horizontal SST gradients could be estimated but T_t could not be estimated, the specification was that of no heat advection, that is, $uT_x + vT_y = 0$. If neither image was cloud-free on the subset, then the kinetic energy was minimized there, that is, $u = 0$ and $v = 0$.

Another change we made was in the computation of the large-scale temperature change term, S . Kelly [1989] computed the S term as part of the inversion, which allowed the SST changes to be distributed between the advective terms and S in a way which optimally minimized the residual m in (2). However, a different S term is required for each image pair, which if incorporated into the original method using multiple image pairs, would substantially increase the program complexity and the computation time. Therefore $S(x, y)$ was computed as the best fit to T_t , the temporal derivative of SST, for each image pair before doing the inversion. To allow more spatial structure, we changed the functional form of S from a linear gradient to biharmonic splines, but with $nd = 7$, which gave spatial scales for S of more than 120 km.

We also removed both the column weighting and the row weighting [Kelly, 1989] in these inversions. Column weighting was necessary in the original version to scale the size of S relative to the temperature gradients; however, because S was computed separately here, the column weighting was unnecessary. The function of row weighting is to prevent large measured values of SST gradients from numerically dominating the solution to the inversion; in other words, the heat equation should be equally valid in regions of large and small gradients. In practice, however, small errors in T_t can produce unrealistically large velocities in regions with small SST gradients. For example, if the actual velocity is zero, then by (4), $T_t' = 0$. However, for an error in T_t' of ϵ , the inversion will attempt to find a solution which satisfies $uT_x + vT_y = \epsilon$; for regions of small horizontal SST gradients, the erroneous velocity will be large. This was not a problem in the original method [Kelly, 1989] because the column scaling factor for S was set large enough to prevent the row from being scaled by negligible SST gradients. Because S

was not part of the inversion here, we eliminated row weighting and allowed the solution to be biased toward regions of large SST gradients, where we expect heat advection to be greatest and where both the neglected terms in (4) and the SST errors are least likely to influence the solutions.

Acknowledgments. K.A.K. gratefully acknowledges the support of the Office of Naval Research on contract N00014-90-J-1808 (Coastal Sciences Division) and contract N00014-86-K-0751 (University Research Initiative). Support for P.T.S. was provided by NASA grant NAGW-1251, JPL contract 958128 and EOS grant NAF-5-30553. The field data were collected during the Coastal Transition Zone program, sponsored by the Office of Naval Research (ONR) through the Coastal Sciences Program (Code 1122CS). Peter Niiler and Ken Brink provided the drifter data, and Steve Ramp and Mike Kosro provided the ADCP data for comparison with the AVHRR velocities. The AVHRR images were provided by the Scripps Satellite Oceanography Center. Altimeter data were provided to P.T.S. by Lee Fu and Victor Zlotnicki at JPL and further processed by Donna Witter and Michael Schlax at Oregon State University. Corinne James processed the images and other data used at Oregon State University. We also thank Steve Lentz and the reviewers, whose suggestions made this manuscript clearer and more concise. Woods Hole Oceanographic Institution contribution 7851.

REFERENCES

- Brink, K.H., and T.J. Cowles, The Coastal Transition Zone program, *J. Geophys. Res.*, *96*, 14,637–14,647, 1991.
- Brink, K.H., R.C. Beardsley, P.P. Niiler, M. Abbott, A. Huyer, S. Ramp, T. Stanton, and D. Stuart, Statistical properties of near surface flow in the California coastal transition zone, *J. Geophys. Res.*, *96*, 14,693–14,706, 1991.
- Bretherton, F.P., R.E. Davis, and C.B. Fandry, A technique for objective analysis and design of oceanographic experiments applied to MODE-73, *Deep Sea Res.*, *23*, 559–582, 1976.
- Caruso, M.J., Z. Sirkes and P.J. Flament, Altimeter processing tools for analyzing mesoscale ocean features, *Tech. Rep. WHOI-90-45*, Woods Hole Oceanogr. Inst., Woods Hole, Mass., 1990.
- Chavez, F.P., R.T. Barber, P.M. Kosro, A. Huyer, S.R. Ramp, T.P. Stanton, and B. Rojas de Mendiola, Horizontal transport and the distribution of nutrients in the coastal transition zone off northern California: effects on primary production, phytoplankton biomass, and species composition, *J. Geophys. Res.*, *96*, 14,833–14,848, 1991.
- Cheney, R.E., B.C. Douglas, R.W. Agreen, L. Miller, D.L. Porter, and N.S. Doyle, Geosat altimeter geophysical data record user handbook, *NOAA Tech. Memo. NOS NGS-46*, 29 pp., Natl. Ocean Serv., Rockville, Md., 1987.
- Collins, M.J., and W.J. Emery, A computational method for estimating sea ice motion in sequential Seasat synthetic aperture radar imagery by matched filtering, *J. Geophys. Res.*, *93*, 9241–9251, 1988.
- Dewey, R.K., J.N. Moum, C.A. Paulson, D.R. Caldwell, and S.D. Pierce, Structure and dynamics of a coastal filament, *J. Geophys. Res.*, *96*, 14,885–14,907, 1991.
- Emery, W.J., A.C. Thomas, M.J. Collins, W.R. Crawford and D.L. Mackas, An objective method for computing advective surface velocities from sequential infrared satellite images, *J. Geophys. Res.*, *91*, 12,865–12,878, 1986.
- Emery, W.J., C. Fowler, and C.A. Clayson, Satellite image derived Gulf Stream currents compared with numerical model results, *J. Atmos. Oceanogr. Technol.*, in press, 1992.
- Garcia, C.A.E., and I.S. Robinson, Sea surface velocities in shallow seas extracted from sequential coastal zone color scanner satellite data, *J. Geophys. Res.*, *94*, 12,681–12,691, 1989.
- Haidvogel, D.B., A. Beckmann, and K.S. Hedström, Dynamical simulations of filament formation and evolution in the coastal transition zone, *J. Geophys. Res.*, *96*, 15,017–15,040, 1991.
- Huyer, A.J., et al., Currents and water masses of the coastal transition zone off northern California, June to August 1988, *J. Geophys. Res.*, *96*, 14,809–14,831, 1991.
- Kamachi, M., Advective surface velocities derived from sequential

- images for rotational flow field: Limitations and applications of maximum cross correlation method with rotational registration, *J. Geophys. Res.*, *94*, 18,227-18,233, 1989.
- Kelly, K.A., Swirls and plumes or applications of statistical methods to satellite-derived sea surface temperatures, *SIO Ref. 83-15, CODE Tech. Rep. 18*, 210 pp., Scripps Inst. of Oceanogr., La Jolla, Calif., 1983.
- Kelly, K.A., An inverse model for near-surface velocity from infrared images, *J. Phys. Oceanogr.*, *19*, 1845-1864, 1989.
- Kelly, K.A., and R.E. Davis, An analysis of errors in sea surface temperature in a series of infrared images from NOAA 6, *J. Geophys. Res.*, *91*, 2633-2644, 1986.
- Kosro, P.M., et al., The structure of the transition zone between coastal waters and the open ocean off northern California, winter and spring, 1987, *J. Geophys. Res.*, *96*, 14,707-14,730, 1991.
- Lagerloef, G.S.E., On the Point Arena Eddy; A recurring summer anticyclone in the California Current, *J. Geophys. Res.*, in press, 1992.
- Niiler, P.P., R.E. Davis, and H.J. White, Water-following characteristics of a mixed layer drifter, *Deep Sea Res.*, *34*, 1867-1881, 1987.
- Rienecker, M.M., C.H. Reed, and C.N.K. Mooers, Mesoscale variability in the California Current system during 1982 to 1986: Maps of surface dynamic height, sea surface temperature, temperature at 50 m, mixed layer depth and depth of the 8°C isotherm from observations during the OPTOMA program, *INO Technical Rep. 87-01*, 138 pp., Inst. of Naval Oceanogr., Bay St. Louis, MS, 1987.
- Sandwell, D.T., Biharmonic spline interpolation of GEOS-3 and Seasat altimeter data, *Geophys. Res. Lett.*, *14*, 139-142, 1987.
- Strub, P.T., et al., The nature of the cold filaments in the California Current system, *J. Geophys. Res.*, *96*, 14,743-14,768, 1991.
- Swenson, M.S., P.P. Niiler, K.H. Brink, and M.R. Abbott, Drifter observations of a cold filament off Point Arena, California in July 1988, *J. Geophys. Res.*, *97*, 3593-3610, 1992.
- Taggart, D.M., Determination of the near-surface velocity fields in the CTZ using combined altimetric and inverse modelling techniques, M.S. thesis, 45 pp., Nav. Postgrad. Sch., Monterey, Calif., 1991.
- Tokmakian, R.T., P.T. Strub, and J. McClean-Padman, Evaluation of the maximum cross-correlation method of estimating sea surface velocities from sequential satellite images, *J. Atmos. Oceanic Technol.*, *7*, 852-865, 1990.
- Vastano, A.C., and S.E. Borders, Sea surface motion over an anticyclonic eddy on the Oyashio Front, *Remote Sens. Environ.*, *16*, 87-90, 1984.
- Wald, L., Predictability of the oceanic current field from routine satellite surveys of the sea-surface temperature field, *CTAMN/83/R/05 - March, 1983*, 76 pp., European Space Agency, 1983.
- Walstad, L.J., J.S. Allen, P.M. Kosro, and A. Huyer, Dynamics of the coastal transition zone in 1987 through data assimilation studies, *J. Geophys. Res.*, *96*, 14,959-14,977, 1991.

K. A. Kelly, Woods Hole Oceanographic Institution, Woods Hole, MA 02543.

P. T. Strub, College of Oceanography, Oregon State University, Corvallis, OR 97331.

(Received November 21, 1991;
accepted January 20, 1992.)